

Article

Novel Non-Centrosymmetric $\text{NdSr}_4\text{O}(\text{BO}_3)_3$ Borate and $\text{Nd}(\text{Ca}_{1-x}\text{Sr}_x)_4\text{O}(\text{BO}_3)_3$ Solid Solutions: Preparation, Crystal Structures, Thermal Expansion and Optical Properties

Rimma Bubnova^{1,2,*}, Valentina Yukhno¹ , Artem Yurev^{1,2}, Alexey Povolotskiy² , Maria Krzhizhanovskaya² , Sergey Volkov^{1,3}, Valery Ugolkov¹ and Stanislav Filatov^{2,*}

¹ Grebenshchikov Institute of Silicate Chemistry, Makarov Emb. 2, St. Petersburg 199034, Russia; yukhno.valentina@gmail.com (V.Y.); artem.yurev@gmail.com (A.Y.); zoom273@inbox.ru (S.V.); ugovkov.52@mail.ru (V.U.)

² Department of Crystallography, Saint Petersburg State University, University Emb. 7/9, St. Petersburg 199034, Russia; apov@inbox.ru (A.P.); krzhizhanovskaya@mail.ru (M.K.)

³ Laboratory of Arctic Mineralogy and Material Sciences, Kola Science Centre, Russian Academy of Sciences, Apatity 184209, Russia

* Correspondence: rimma_bubnova@mail.ru (R.B.); filatov.stanislav@gmail.com (S.F.)

Abstract: A novel non-centrosymmetric $\text{NdSr}_4\text{O}(\text{BO}_3)_3$ borate and solid solutions of $\text{Nd}(\text{Ca}_{1-x}\text{Sr}_x)_4\text{O}(\text{BO}_3)_3$ ($x = 0.0, 0.1, 0.2, 0.3, 0.4, 0.5, 0.7, 1.0$) were synthesized by solid-state reactions as well as crystallization from a melt. The crystal structures of the $\text{Nd}(\text{Ca}_{1-x}\text{Sr}_x)_4\text{O}(\text{BO}_3)_3$ solid solutions with $x = 0.2, 0.5$ and 1.0 were determined from single crystal X-ray diffraction data and refined in the monoclinic space group Cm to $R_{\text{obs}} = 0.028, 0.034$ and 0.028 , respectively. The thermal expansion of the samples with $x = 0, 0.2$ and 0.5 was investigated using powder high-temperature X-ray diffraction in the temperature range of $25\text{--}1000$ °C. A similarity of the thermal and compositional (Ca-Sr substitution) deformations of $\text{Nd}(\text{Ca}_{1-x}\text{Sr}_x)_4\text{O}(\text{BO}_3)_3$ solid solutions is revealed: Heating of $\text{Nd}(\text{Ca}_{0.5}\text{Sr}_{0.5})_4\text{O}(\text{BO}_3)_3$ by 1 °C leads to the same deformations of the crystal structure as increasing the amount of Sr atoms in $\text{Nd}(\text{Ca}_{0.5}\text{Sr}_{0.5})_4\text{O}(\text{BO}_3)_3$ by 0.26 at% Sr. The SHG signal of the series of $\text{Nd}(\text{Ca}_{1-x}\text{Sr}_x)_4\text{O}(\text{BO}_3)_3$ solid solutions has a maximum at approximately $x = 0.2$.

Keywords: borates; crystal structure; thermal expansion; solid solutions; second-harmonic generation; non-linear optical materials



Citation: Bubnova, R.; Yukhno, V.; Yurev, A.; Povolotskiy, A.; Krzhizhanovskaya, M.; Volkov, S.; Ugolkov, V.; Filatov, S. Novel Non-Centrosymmetric $\text{NdSr}_4\text{O}(\text{BO}_3)_3$ Borate and $\text{Nd}(\text{Ca}_{1-x}\text{Sr}_x)_4\text{O}(\text{BO}_3)_3$ Solid Solutions: Preparation, Crystal Structures, Thermal Expansion and Optical Properties. *Crystals* **2023**, *13*, 1395. <https://doi.org/10.3390/cryst13091395>

Academic Editor: Yael Diskin-Posner

Received: 21 August 2023

Revised: 11 September 2023

Accepted: 13 September 2023

Published: 19 September 2023



Copyright: © 2023 by the authors. Licensee MDPI, Basel, Switzerland. This article is an open access article distributed under the terms and conditions of the Creative Commons Attribution (CC BY) license (<https://creativecommons.org/licenses/by/4.0/>).

1. Introduction

The calcium lanthanide oxyborates with the general formula of $\text{LnCa}_4\text{O}(\text{BO}_3)_3$ ($\text{Ln} = \text{Y}, \text{La}\text{--}\text{Lu}$) (LnCOB) became the focus of a number of studies. These oxoborates were first described by Khamaganova et al. [1]. They crystallized in the monoclinic system, space group Cm [1–3]. Research [4–10] showed that the family of LnCOB borates is a source of crystals with good NLO properties. The LnCOB is comparable with well-known active media, such as Nd-activated $\text{YAl}_3(\text{BO}_3)_4$, $\text{LaSc}_3(\text{BO}_3)_4$, and $(\text{Ce},\text{Gd})\text{Sc}_3(\text{BO}_3)_4$, in lasing and non-linear optical properties [11–13]. It has been reported that $\text{GdCa}_4\text{O}(\text{BO}_3)_3$ (GdCOB), $\text{YCa}_4\text{O}(\text{BO}_3)_3$ (YCOB) and solid solutions of $\text{Gd}_x\text{Y}_{1-x}\text{Ca}_4\text{O}(\text{BO}_3)_3$ (GdYCOB) are suitable for blue to near-UV generation [14–18]. GdYCOB crystal is unique in that its birefringence is tunable by controlling the composition ratio of Gd to Y. The optical non-linearity of a crystal can be improved through doping processes, for example, with partial substitution of Yb for Y in $\text{YCa}_4\text{O}(\text{BO}_3)_3$ [19].

The crystal structure of $\text{LnCa}_4\text{O}(\text{BO}_3)_3$ consists of $M1\text{--}M3$ octahedra ($M = \text{Ca}^{2+}, \text{Ln}^{3+}$) and BO_3 trigonal planar groups [1,2,20]; the $M3$ polyhedra can be described as eightfold polyhedra [13,21]. Ions occupied these positions partially orderly: rare earths elements filled mainly the $M1$ positions, calcium— $M2$ and $M3$. Currently, there are studies of structures in which Ca^{2+} ions are replaced by other metal ones, mainly Sr^{2+} ; the effect of these

substitutions on various properties has been studied [22–24]. According to Liu et al. [22], the NLO properties of $\text{GdCa}_4\text{O}(\text{BO}_3)_3$ crystals can be significantly improved by doping with 4% Sr^{2+} . The SHG efficiency achieved with Sr-doped and undoped $\text{GdCa}_4\text{O}(\text{BO}_3)_3$ was 37 and 28%, respectively. It was shown in [24] that 35% of Sr ions can be incorporated instead of Ca into $\text{Gd}(\text{Ca}_{1-x}\text{Sr}_x)_4\text{O}(\text{BO}_3)_3$ solid solutions. Moreover, by adjusting the Sr content in $\text{La}(\text{Ca}_{1-x}\text{Sr}_x)_4\text{O}(\text{BO}_3)_3$ crystals ($x = 0\text{--}0.4$), the optical birefringence can be controlled and the blue light can be obtained in the range of 495–473 nm through type-I NCPM SHG of the corresponding fundamental wavelengths [23]. Wide ranges of Ca \rightarrow Sr substitution are due to the closeness of the ionic radii of Ca^{2+} and Sr^{2+} (1.14 Å and 1.32 Å, respectively, for coordination number 6 [25]) and this maintains the congruent melting property, enabling the production of high-quality crystals. At the same time, the combination of coupled substitution with Na and REE is very limited, and the combination of Ca with Sr, Na and Gd could not be synthesized [24].

Some studies on $\text{LnCa}_4\text{O}(\text{BO}_3)_3$ have focused on a variety of properties: melting points [2,21,26], thermal expansion [27], photoluminescence [28–31], thermal conductivity [27], dielectric, elastic and piezoelectric behavior [26,32,33] and magnetism [20,34]. However, thermal expansion of the $\text{LnCa}_4\text{O}(\text{BO}_3)_3$ family is poorly studied; there are only thermal expansion coefficients along the crystallographic axes for $\text{GdCa}_4\text{O}(\text{BO}_3)_3$ [27], which is insufficient to characterize an anisotropy of thermal expansion for a monoclinic crystal. In the case of oblique crystals, it is necessary to calculate the principal values of the thermal expansion tensor in order to study the expansion anisotropy. In addition, LnCOB has shown itself to be a promising material for efficient non-linear frequency conversion through non-critical phase matching (NCPM), and ongoing research is exploring its potential applications in optical technology [23]. The family of rare earth calcium oxoborates, LnCOB , contains promising candidates for pyro- and piezoelectric applications; their use is not limited to phase transitions [24]. Due to its congruent melting and absence of phase transitions, it can be grown from the melt directly and used in pyro- and piezoelectrics.

Here, in order to investigate the influence of cation substitutions on NLO properties and to expand the RCOB ($R = \text{REE}$) family, we report the results of synthesis and complex investigations of new NLO $\text{Nd}(\text{Ca}_{1-x}\text{Sr}_x)_4\text{O}(\text{BO}_3)_3$ solid solutions and a new $\text{NdSr}_4\text{O}(\text{BO}_3)_3$ compound. In the series of $\text{NdCa}_4\text{O}(\text{BO}_3)_3$ compounds, it was possible to almost double the Ca \rightarrow Sr substitution limits for Nd (x is approximately 0.7) in comparison to Gd ($x = 0.35$) and La ($x = 0.4$) [24]. In addition, a new non-centrosymmetric $\text{NdSr}_4\text{O}(\text{BO}_3)_3$ compound obtained in the present studies can be considered as the prototype of a new $\text{REESr}_4\text{O}(\text{BO}_3)_3$ series, where doped additives can be introduced into the position of a rare earth element to study the luminescent properties of these multifunctional materials.

2. Materials and Methods

2.1. Synthesis

Polycrystalline samples of $\text{Nd}(\text{Ca}_{1-x}\text{Sr}_x)_4\text{O}(\text{BO}_3)_3$ ($x = 0; 0.1; 0.2; 0.3; 0.4; 0.5; 0.7; 0.8; 0.9; 1$) were synthesized by multi-step solid-state reactions from CaCO_3 , SrCO_3 , Nd_2O_3 and H_3BO_3 (99.90% purity). Boric acid was added with an excess of 3% as noted in [24]. To remove the adsorption moisture, the reagents were pre-calcined: strontium and calcium carbonate at 600 °C/6 h, neodymium oxide at 800 °C/3 h. After homogeneous grinding and mixing in an agate mortar for 1 h, tablets were pressed from the powder using a hydraulic press at a pressure of 80 kg/cm², after the tablet was heated at 900 °C for 9 h. The polycrystalline products with the common formula $\text{Nd}(\text{Ca}_{1-x}\text{Sr}_x)_4\text{O}(\text{BO}_3)_3$ were synthesized by a three-step sintering process. The first step was heating tablets in a platinum crucible at 1200 °C and exposing them for 30 h with slow cooling in the Nabertherm HTC furnace. In the second step, heating was carried out to 1300 °C for 60 h, followed by slow cooling in the furnace by switching off the furnace. The last step was heating at 1350 °C with exposure for half an hour. All powder samples were examined by means of X-ray powder diffraction (XRD). To obtain small single crystals, the samples were heated in

platinum crucibles above melting temperature of 1430 °C for half an hour, after which they were slowly cooled in the furnace.

2.2. Powder X-ray Diffraction

Powder diffraction data of the $\text{Nd}(\text{Ca}_{1-x}\text{Sr}_x)_4\text{O}(\text{BO}_3)_3$ samples after three heat treatments were collected using a Rigaku MiniFlex II diffractometer ($\text{CuK}\alpha$, $2\theta = 10\text{--}70^\circ$, step 0.02°). The phase composition was determined using PDXL-integrated X-ray powder diffraction software and PDF-2 2016 (ICDD) database [35]. Quantitative phase analysis of the samples and unit cell parameters of $\text{Nd}(\text{Ca}_{1-x}\text{Sr}_x)_4\text{O}(\text{BO}_3)_3$ solid solutions were refined by Rietveld method in the RTT program software [36]. X-ray powder diffraction patterns of the $\text{Nd}(\text{Ca}_{1-x}\text{Sr}_x)_4\text{O}(\text{BO}_3)_3$ samples after heat treatment at 1300 °C are given in Figure S1.

2.3. Single Crystal X-ray Diffraction

Single crystals of $\text{Nd}(\text{Ca}_{1-x}\text{Sr}_x)_4\text{O}(\text{BO}_3)_3$, $x = 0.2, 0.5$ were selected in polarized light using an optical microscope and attached to a glass fiber using epoxy glue. The experimental data were collected on a Bruker Apex II diffractometer utilizing $\text{MoK}\alpha$ radiation. Lorentz and polarization corrections were applied. The absorption correction based on a crystal shape was performed. The structures were solved using a charge-flipping method [37] implemented in JANA2006 [38]. The structures could be refined to $R_{\text{obs}} = 0.028, 0.034$ and 0.28 for $x = 0.2, 0.5$ and 1.0 , respectively. Details of data collection and structure refinement are summarized in Table 1. Atomic coordinates, occupancies and atomic anisotropic displacement parameters are given in Tables S1–S6, selected bond lengths are in Table S7. Further details of the crystal structure investigations can be obtained from the Cambridge Structural Database by quoting the depository numbers CSD 2286252 ($\text{NdCa}_{3.2}\text{Sr}_{0.8}\text{O}(\text{BO}_3)_3$), 2286231 ($\text{NdCa}_2\text{Sr}_2\text{O}(\text{BO}_3)_3$) and 2286250 ($\text{NdSr}_4\text{O}(\text{BO}_3)_3$). Data visualization was performed with the Vesta 3 [39] software.

Table 1. Crystal data and experimental details for structures of $\text{Nd}(\text{Ca}_{1-x}\text{Sr}_x)_4\text{O}(\text{BO}_3)_3$ ($x = 0, 0.2, 0.5, 1$) solid solutions.

x_{Sr}	0.0 [21]	0.2 *	0.5 *	1.0 *
Crystal data				
M_r		535	592.1	687.1
Crystal system, space group, Z	Monoclinic, Cm , 2			
Temperature (K)	293			
a (Å)	8.12367 (5)	8.1882 (2)	8.2832 (3)	8.3311 (2)
b (Å)	16.04587 (9)	16.1822 (4)	16.3631 (6)	16.4552 (4)
c (Å)	3.595667 (19)	3.6238 (1)	3.6797 (2)	3.7085 (1)
β (°)	101.3937 (4)	101.444 (2)	101.671 (4)	101.767 (2)
V (Å ³)	459.457 (4)	470.62 (2)	488.43 (4)	497.71 (2)
Radiation type	Mo $K\alpha$			
μ (mm ^{−1})		17.21	11.79	26.46
Crystal size (mm)		$0.2 \times 0.4 \times 0.3$	$0.2 \times 0.4 \times 0.2$	$0.3 \times 0.2 \times 0.1$

Table 1. Cont.

x_{Sr}	0.0 [21]	0.2 *	0.5 *	1.0 *
Data collection				
Diffractometer	XtaLAB Synergy, single source at home/near, HyPix			
Absorption correction	Multi-scan			
No. of measured, independent and observed [$I > 3\sigma(I)$] reflections		1683, 1682, 1655	1361, 1360, 1285	22454, 2447, 2416
R_{int}		0.03	0.04	0.045
$(\sin \theta / \lambda)_{\text{max}}$ (\AA^{-1})		0.778	0.703	0.848
Refinement				
$R[F^2 > 2\sigma(F^2)], wR(F^2), S$		0.028, 0.035, 2.05	0.034, 0.043, 2.25	0.028, 0.038, 3.12
No. of reflections		1682	1360	2447
No. of parameters		88	85	84

* Present work.

2.4. High-Temperature Single-Crystal X-ray Diffraction

The temperature-dependent structural behavior of $\text{Nd}(\text{Ca}_{0.8}\text{Sr}_{0.2})_4\text{O}(\text{BO}_3)_3$ solid solution ($x = 0.2$) under heating in the air was studied in situ by high-temperature single-crystal X-ray diffraction using a XtaLAB Synergy-S diffractometer (Rigaku Oxford Diffraction, Japan) operated with monochromated $\text{MoK}\alpha$ radiation ($\lambda[\text{MoK}\alpha] = 0.71073 \text{ \AA}$) at 50 kV and 40 mA and equipped with an HyPix-6000HE detector with a unique high-temperature FMB Oxford system. The sample heating is performed using a gas blower up to 1000 (± 1) $^\circ\text{C}$, which consists of a hot air generator controlled by a Eurotherm regulator and gas flow controller. For this experiment, the single crystal with an approximate size of $30 \mu\text{m} \times 20 \mu\text{m} \times 40 \mu\text{m}$ was mounted on the glass fiber, which was placed into the quartz capillary. Diffraction data were collected at different temperatures without changing the orientation of the crystal in the range of 27–1000 $^\circ\text{C}$ with a temperature step of 100 $^\circ\text{C}$. The crystal structures were refined at 11 temperatures, including room temperature after heating. Crystal data and experimental details for 6 are given in Table S8, selected bond lengths are in Table S9. Anisotropic displacement parameters were refined for all atoms.

2.5. High-Temperature Powder X-ray Diffraction

Homogeneous solid solutions of $\text{Nd}(\text{Ca}_{1-x}\text{Sr}_x)_4\text{O}(\text{BO}_3)_3$, $x = 0, 0.2, 0.5$, were investigated by X-ray powder diffraction at high temperatures using the Rigaku Ultima IV diffractometer ($\text{CuK}\alpha_{1+2}$, 40 kV/30 mA, 25–1000 $^\circ\text{C}$, temperature step of 20 $^\circ\text{C}$, Rigaku R-300 high-temperature attachment). A Pt-Pt/Rh thermocouple was used to control the temperature. As an example, a 2D-top view of HTXRD pattern of the sample $\text{Nd}(\text{Ca}_{0.5}\text{Sr}_{0.5})_4\text{O}(\text{BO}_3)_3$ is presented in Figure S2. Multi-stage processing of experimental data was carried out using the RietveldToTensor 2.0 software [37]. The first step included the refinement of the unit cell parameters and quantitative phase composition at different temperatures by the Rietveld method using the room-temperature crystallographic information file (CIF) obtained in this work from single-crystal XRD data as a model for Rietveld refinement. Then temperature dependences of unit-cell parameters and volume were approximated by polynomial functions for all samples (Table S10), the components of the tensor (α_{ij}) of thermal expansion were determined in a Cartesian crystal-physical coordinate system using the coefficients of approximation and finally drawing figures of thermal expansion coefficients (α) were performed in the RietveldToTensor software. A detailed description of the data processing and calculation of eigenvalues of thermal expansion tensor is given in [36]. Standard orientation of the crystallographic axes (set II for monoclinic systems)

with respect to the crystal-physical axes has been used. The eigenvalues of the tensors of thermal expansion and TECs along crystallographic axes were calculated (see Table 3), and the latter are compared to the results obtained in [27].

2.6. Thermal Analysis

The high-temperature behavior was studied by differential scanning calorimetry (DSC) and thermogravimetry (TG) on a NETZSCH STA 429 thermal analyzer. Measurements were performed on tablets containing approximately 20–50 mg placed in a Pt-Rh crucible. The heating and cooling rate was 20 °C/min in the heating range of 20–1450 °C and then cooled at 900 °C. For example, microphotographs of the tablet of $\text{NdCa}_4\text{O}(\text{BO}_3)_3$ in the Pt crucible before (left) and after (right) heating to 1445 °C are given in Figure S3. The temperatures of the thermal effects were estimated as the first derivative onset temperatures, when possible, and as maximum temperatures in the case of multiple peaks overlapping. According to the TG data, very small mass losses gradually occurred during heating, apparently due to the high heating rate.

2.7. Spectroscopy

UV–Vis absorption spectra were measured using a PerkinElmer Lambda 1050 spectrophotometer equipped with a 150-mm integrated sphere. Barium sulfate (BaSO_4) sample was used as a blank. Raman spectra were collected with a Horiba LabRam HR800 spectrometer at 632.8 nm excitation.

2.8. Second Harmonic Generation (SHG) Measurements

SHG measurements were made using the Kurtz–Perry method against polycrystalline α -quartz (grain size of 0.07–0.5 μm). A 31-A femtosecond Ti:Sapphire amplifier with a pulse energy of 1 mJ, pulse duration of 35 fs and repetition rate of 1 kHz as a source of radiation at $\lambda\omega = 800$ nm was used. The SHG signal was registered in reflection mode and measured by a spectrometer based on a single monochromator M266 and multichannel CCD detector UC-12T3.

3. Results

3.1. Powder X-ray Diffraction Studies

After heat treatment at 1200 °C, the samples of $\text{Nd}(\text{Ca}_{1-x}\text{Sr}_x)_4\text{O}(\text{BO}_3)_3$ were homogeneous in the range of x_{Sr} compositional parameter $x = 0$ –0.3, and peaks corresponded to the XRD patterns of $\text{LnCa}_4\text{O}(\text{BO}_3)_3$ borate in accordance with the data (PDF-2 ICDD). The samples with $x = 0.4$ and 0.5 contained a few additional peaks of $\text{Sr}_3\text{B}_2\text{O}_6$. After heat treatment at 1300 °C, the samples of $\text{Nd}(\text{Ca}_{1-x}\text{Sr}_x)_4\text{O}(\text{BO}_3)_3$ were homogeneous up to $x = 0.5$ and the sample with $x = 0.7$ contained approximately 7 wt % of $\text{Sr}_3\text{B}_2\text{O}_6$ as an impurity (Figure S1). The substitution of Ca by Sr shows that Sr can be incorporated up to an amount of 70 at. % and homogeneous solid solutions were found for $x_{\text{Sr}} = 0$ –0.7. With further increasing content, the peaks of $\text{Sr}_3\text{B}_2\text{O}_6$ and NdBO_3 could appear in the PXRD patterns: in the sample with $x_{\text{Sr}} = 0.8$, the content of the $\text{Nd}(\text{Ca}_{1-x}\text{Sr}_x)_4\text{O}(\text{BO}_3)_3$ solid solution ($x \sim 0.7$) decreased to approximately 65 wt % respectively, while the $\text{Sr}_3\text{B}_2\text{O}_6$ content increased to approximately 25 wt % and additional peaks of unidentified phase were observed (Figure S1). In the PXRD pattern of the sample with $x = 0.9$, the content of the $\text{Nd}(\text{Ca}_{1-x}\text{Sr}_x)_4\text{O}(\text{BO}_3)_3$ solid solution ($x \sim 0.7$) decreased gradually to 50 wt %, $\text{Sr}_3\text{B}_2\text{O}_6$ and NdBO_3 appeared at approximately 25 and 25 wt %. After heat treatment at 1350 °C, the $\text{Nd}(\text{Ca}_{1-x}\text{Sr}_x)_4\text{O}(\text{BO}_3)_3$ solid solutions were homogeneous in the same region as the compositional parameter ($x = 0.5$); the sample with $x = 0.7$ also contained a solid solution and approximately 7% of $\text{Sr}_3\text{B}_2\text{O}_6$ borate. Multi-phase samples ($x = 0.8, 0.9$) melted and contained at least three phases: the $\text{Nd}(\text{Ca}_{1-x}\text{Sr}_x)_4\text{O}(\text{BO}_3)_3$ solid solutions ($x \sim 0.7$), $\text{Sr}_3\text{B}_2\text{O}_6$ and NdBO_3 . Thus, the miscibility range can be estimated to be $x_{\text{Sr}} \sim 0$ –0.7. This is almost twice the $\text{Ca} \rightarrow \text{Sr}$ substitutions in the $\text{Gd}(\text{Ca}_{1-x}\text{Sr}_x)_4\text{O}(\text{BO}_3)_3$ series [24]. The PXRD pattern

of novel $\text{NdCa}_4\text{O}(\text{BO}_3)_3$ borate ($x = 1$) contained also the $\text{Sr}_3\text{B}_2\text{O}_6$ admixture in an amount of approximately 8 wt %.

The unit cell parameters of $\text{Nd}(\text{Ca}_{1-x}\text{Sr}_x)_4\text{O}(\text{BO}_3)_3$ solid solutions after heat treatment at 1300°C increase almost linearly with the gradual growth of Sr^{2+} content to $x = 0.7$ (Figure 1) according to the larger ionic radii of Sr^{2+} ([6] 1.32 \AA) ions in comparison to Ca^{2+} ([6] 1.14 \AA) ones [25]. The parameter c increases most strongly, while a and b change insignificantly, and the monoclinic angle increases by 0.4° . With a further increase in the content of strontium ions ($x > 0.7$), a multi-phase region appears in which the parameters remain practically unchanged to $x = 1$ (Figure 1), which may indicate the stability of the new $\text{NdSr}_4\text{O}(\text{BO}_3)_3$ phase. The parameters determined from powder and single-crystal XRD data (Figure 1, open and filled circles) are in good agreement.

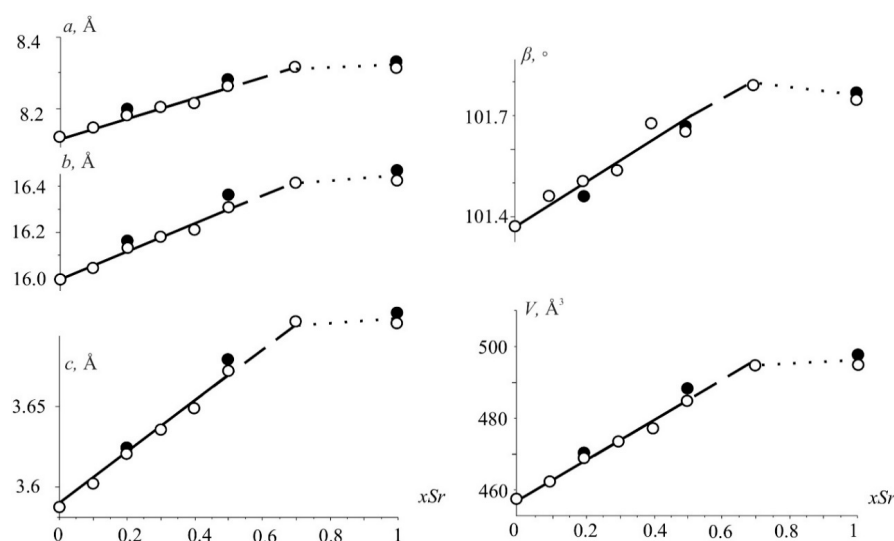


Figure 1. The unit-cell parameters and the volume versus Sr-content in the $\text{Nd}(\text{Ca}_{1-x}\text{Sr}_x)_4\text{O}(\text{BO}_3)_3$ solid solution. Values obtained from powder and single-crystal XRD data are shown with open and filled circles.

3.2. Crystal Structures of $\text{Nd}(\text{Ca}_{1-x}\text{Sr}_x)_4\text{O}(\text{BO}_3)_3$ Solid Solutions

There are three M1–M3 sites for Nd and Ca and Sr cations, B1 and B2 and O1–O6 sites in asymmetric units in the series of $\text{Nd}(\text{Ca}_{1-x}\text{Sr}_x)_4\text{O}(\text{BO}_3)_3$ solid solutions (Tables S1–S6). The cations are distributed over the three sites (Tables 2 and S1–S3): in the $\text{Nd}(\text{Ca}_{1-x}\text{Sr}_x)_4\text{O}(\text{BO}_3)_3$ solid solutions ($x = 0.2, 0.5$) Nd^{3+} ions are situated at the M1 (2a) and M3 (4b) crystallographic sites; the Sr^{2+} ions occupy the two M2 (4b) and M3 (4b) sites, while Ca^{2+} occupy all three sites; in the new $\text{NdSr}_4\text{O}(\text{BO}_3)_3$ compound cations are ordered, Nd^{3+} ions occupy only the M1 (2a) site, Sr—M2 (4b) and M3(4b) ones. This distribution of the cations over the three sites agrees with the bond valence sum (BVS) of the sites (Table 2). For instance, in the case of solid solutions, the BVS (M1) is less than 3, since, in addition to Nd^{3+} , the position is partially filled with Ca^{2+} , while in the $\text{NdSr}_4\text{O}(\text{BO}_3)_3$ borate, the BVS (M1) is closer to 3 due to ordering cation distribution.

The crystal structures of $\text{Nd}(\text{Ca}_{1-x}\text{Sr}_x)_4\text{O}(\text{BO}_3)_3$ borates consist of four groups: M1, M2, M3 polyhedra and two independent isolated $[\text{BO}_3]^-$ groups (Figure 2a). In all structures, M1 and M2 are both six-coordinated polyhedra and M3 is an eightfold-coordinated one. While two of the eight M3—O bond lengths are significantly longer than the other six (Table S7), the M3 site may be treated as eight-coordinated. In the compounds, the ‘long’ M3—O bond lengths are all greater than 2.90 \AA whereas the other bonds range $2.35\text{--}2.65$ for $x = 0.2$ and $2.39\text{--}2.71\text{ \AA}$ for $x = 0.5$ (Table S7). The M1–M3 polyhedra are either edge or corner-connected. There are three edge-linked polyhedral chains along the c axis: M1 octahedra are connected via O1—O6 edges to form single chains; M2 and M3 polyhedra—via O2—O3 and O4—O5 edges to form double chains (Figure 2a, bottom),

respectively. These chains are connected by the vertices of the polyhedra to form a cationic framework. The $M3O_8$ polyhedra share edges with trigonal planar $[BO_3]^-$ groups, which are tilted at different angles relative to the ab -plane.

Table 2. The average bond lengths $M-O$ (Å) and occupancies of M sites in $Nd(Ca_{1-x}Sr_x)_4O(BO_3)_3$ solid solutions.

x_{Sr}	0 [21]	0.2	0.5	1.0
$\langle M1-O \rangle_6 / BVS$	2.393	2.404/2.665	2.414/2.561	2.422/2.729
$\langle M2-O \rangle_6 / BVS$	2.354	2.375/2.185	2.413/2.228	2.435/2.385
$\langle M3-O \rangle_8 / BVS$	2.556	2.586/1.970	2.628/1.992	2.649/1.981
$\langle B1-O \rangle_3 / BVS$	1.381	1.376/2.957	1.379/2.933	1.366/2.968
$\langle B2-O \rangle_3 / BVS$	1.381	1.378/2.944	1.381/2.921	1.379/2.923
M1: Occ Nd	0.942 (8)	0.8977	0.8728	1.0
Occ Ca	0.058	0.1023	0.1272	0.0
Occ Sr	0.0	0.0	0.0	0.0
M2: Occ Nd	0.013	0	0	0
Occ Ca	0.987	0.8096	0.5303	0
Occ Sr	0	0.1904	0.4697	1.0
M3: Occ Nd	0.017	0.0511	0.0636	0
Occ Ca	0.983	0.7393	0.4061	0
Occ Sr	0	0.2096	0.5303	1.0

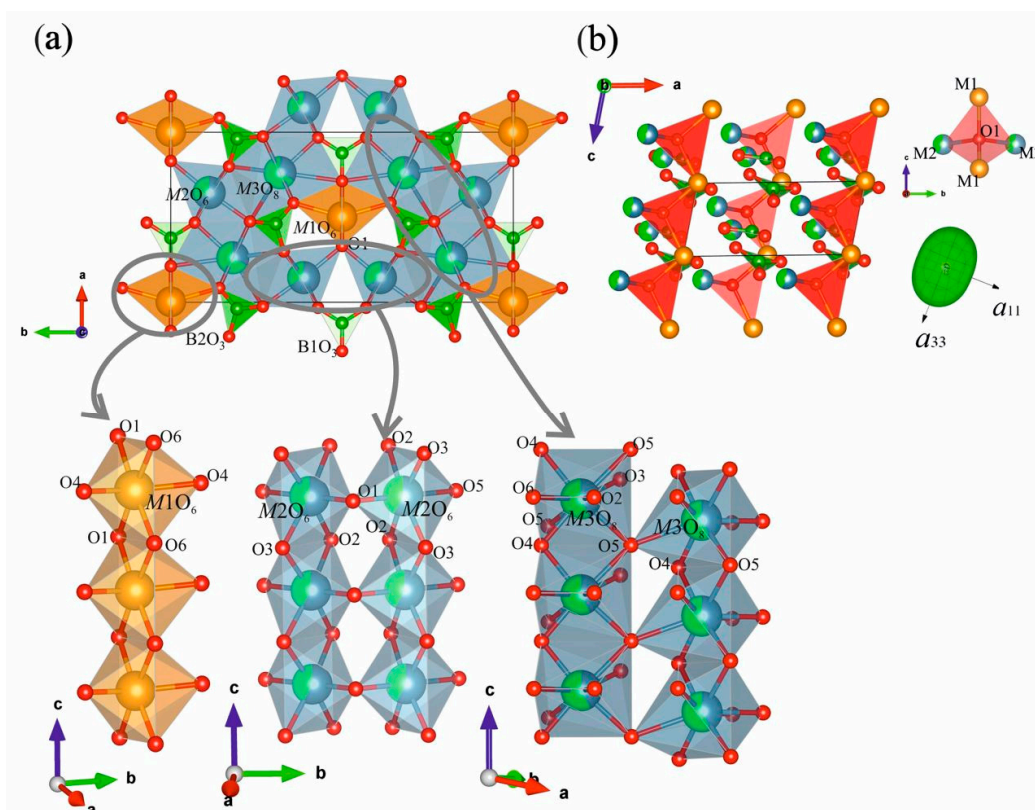


Figure 2. View of the $Nd(Ca_{0.5}Sr_{0.5})_4O(BO_3)_3$ crystal structure in terms of cation-centered polyhedral along the c axis (a, top left), chains of M1–M3 edge-shared polyhedra extended along the c axis (a, bottom left), the $Nd(Ca_{0.5}Sr_{0.5})_4O(BO_3)_3$ structure in the ac -plane in terms of oxy-centered polyhedra (b) and the figures of thermal expansion tensor of this solid solution.

Upon the $Ca \rightarrow Sr$ substitutions, the average bond length in the $M1O_6$ octahedra is practically constant. It increases by 0.03 \AA , while the average bond lengths in $M2O_6$ and

in $M3O_8$ polyhedra increase by 0.08 Å and 0.09 Å, i.e., approximately three times more (Tables 2 and S7). The $\langle M2-O \rangle$ average bond length increases from 2.354 Å [20] to 2.435 Å, $\langle M3-O \rangle$ —from 2.556 Å to 2.65 Å, while the $\langle M1-O \rangle$ bond length in $M1O_6$ polyhedra— from 2.40 to 2.42 Å (Figure 3 bottom left, Tables 2 and S7). Individual bond lengths change more sharply a few of them are even reduced, such as $d(M1-O_4)$ decreased by -0.03 Å. The bonds located close to the c axis and connecting the polyhedra in chains, for example, the $M1-O_6$ bonds by 0.12 Å, $M2-O_1$ by 0.08 Å, and the $M3-O_5$ by 0.06 Å, are more elongated. This correlates with the maximum γ_{33} axis of the compositional deformation tensor, which is also located close to the c axis (see § 3.3.2). While the contracting bonds are located near the perpendicular direction, the chains, expanding in a direction close to the c axis, have to contract in the framework slightly.

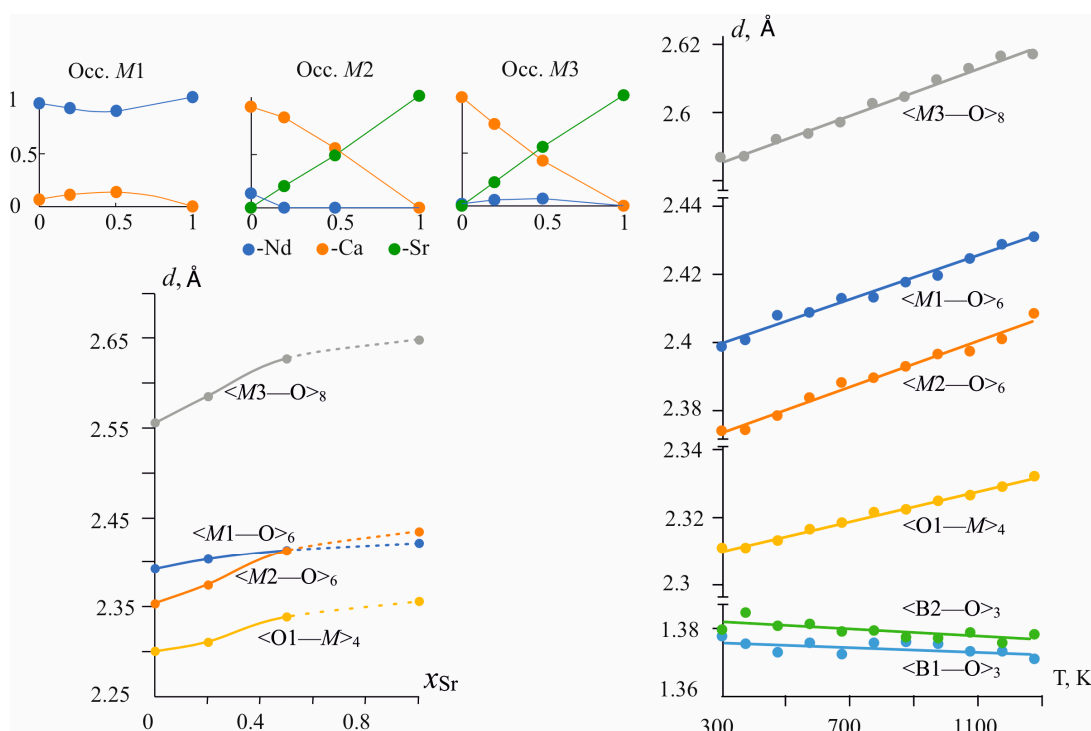


Figure 3. Distribution of cations over $M1$ – $M3$ positions (top left), changes of average bond lengths in the cationic $M1$ – $M3$ polyhedra and oxy-centered OM_4 tetrahedra versus chemical composition (bottom left) and temperature (right).

The reason for structural changes is obvious in the partially ordered substitution of Ca^{2+} by Sr^{2+} ions in the $M1$ – $M3$ positions. Since the $M1$ position is predominantly occupied by Nd^{3+} ions, the substitution does not strongly affect the average bond length in the $M1O_6$ polyhedron. As Ca^{2+} ions are replaced by Sr^{2+} ones, the latter are gradually distributed over the $M2$ and $M3$ positions approximately equally (Figure 3 top left), although among $M1$ – $M3$ polyhedra it is the $M3O_8$ polyhedron that is the largest and most distorted, i.e., it could be expected that it would be mainly filled with strontium. Note that in $NdCa_4O(BO_3)_3$ $M2O_6$ is the smallest and least distorted octahedron; however, it becomes larger than the $M1O_6$ octahedron (Figure 3 bottom left), as Ca^{2+} ions are replaced by Sr^{2+} ones due to the larger size of Sr^{2+} ions. In the case of solid solutions, the Ca, Sr and Nd cations are more randomly distributed over the $M1$ – $M3$ sites than in the new $NdSr_4O(BO_3)_3$ borate, in which they are completely ordered. In the RCOB family, REE and Ca cations are completely ordered in the case of large REE ions, such as La [40] (ICSD #93152); [41] (ICSD #180596), and they are disordered as the radii of REE decrease [20]. For instance, for $LuCa_4O(BO_3)_3$ [3] (ICSD #39718), the cationic distribution is the following: Occ $M1$ 0.64, Ca 0.36; $M2$: Ca 0.82, Lu 0.18; $M3$ Ca 1.

Both $[\text{BO}_3]^-$ triangles are tilted at different angles from the ab -plane. The tiltings of each of these borate groups are 12.66° and 34.59° for $x = 0.2$, 13.53° and 34.78° for $x = 0.5$, and 13.23 and 34.32 for $x = 1.0$. Some studies [34,42] found that the tilting of these borate groups changed regularly as the size of the lanthanide ions varied.

There are O1 oxygen atoms not linked with boron. Hence, this crystal structure can be described in terms of oxy-centered polyhedra (Figure 1b). Additional oxygen atoms have $[\text{O}(1)\text{M}(1)_2\text{M}(2)_2]$ tetrahedral coordination and form corner-shared chains along the c axis. Compared to an increase in average bond lengths in M1-M3 polyhedra, the average bond length in OM_4 tetrahedra increases weaker (Figure 3 bottom left) hence, an oxy-centered OM_4 tetrahedron could be considered as the rigid structural unit. A weak increase of the tetrahedron is caused by the substitution of smaller Ca atoms with larger Sr ones in the M2 position, which leads to the elongation of O1—M2 bonds and an increasing c parameter.

The major contribution to the optical non-linearity originates from the $[\text{BO}_3]^-$ groups that form delocalized π -type bonds perpendicular to the $[\text{BO}_3]$ plane. The CaO_6 octahedra share corners with the $[\text{BO}_3]$ group. The Sr—O—B bonding angles will be more stretched compared to the Ca—O—B bonding since the radius of the Sr^{2+} ion is larger than that of the Ca^{2+} ion, resulting in a more distorted p-type electron cloud in the BO_3 group. The M1—O4—B2 angles are equal to 109.8° , 111.9° and 113.4° ; M3—O5—B2— 121.8° , 123.1° and 121.6° for $x = 0.2$, 0.5 and 1, respectively. The other bond angles vary within the error. It is possible that these changes in angles affect the π -bonds of borate triangles and, accordingly, their non-linear optical properties.

3.3. Compositional versus Thermal Properties in $\text{Nd}(\text{Ca}_{1-x}\text{Sr}_x)_4\text{O}(\text{BO}_3)_3$ Solid Solutions

It is well known [43–47] that in compounds with a mainly ionic character, the replacement of a smaller cation by a bigger one changes the crystal structure in a similar way to heating. The coefficient of the thermal expansion $\alpha_a = (1/a)(da/dt)$ is analogous to the coefficient of the compositional deformation $\gamma_a = (1/a)(da/dx)$, where x , the compositional parameter, is a characteristic of the chemical composition [46]. Thus, we can calculate the compositional equivalents of the thermal expansion [46].

3.3.1. Thermal Expansion

The thermal behavior of $\text{Nd}(\text{Ca}_{1-x}\text{Sr}_x)_4\text{O}(\text{BO}_3)_3$ solid solutions with $x = 0, 0.2$ and 0.5 was investigated within a temperature range of $25\text{--}1000^\circ\text{C}$ from powder HTXRD data. Within this range, only the diffraction peaks of the $\text{Nd}(\text{Ca}_{1-x}\text{Sr}_x)_4\text{O}(\text{BO}_3)_3$ solid solutions were observed for $x = 0$ and 0.2 , while for $x = 0.5$, with further heating above 900°C , weak additional reflections marked as stars in Figure S2 appeared in the HTXRD patterns at approximately 900°C . Apparently, this solid solution starts to decompose. By the way, anomalies in the HTXRD patterns at approximately 900°C were noted in [27].

The unit cell parameters increase in heating from 25°C to 1000°C for all phases (Figure 4). For $x = 0.5$, a distinctive convex bend was found in the range of $400\text{--}600^\circ\text{C}$ in the temperature dependence of the monoclinic β angle. The deviation from the “linear” growth of the parameters can probably be caused by the redistribution of Nd^{3+} , Ca^{2+} and Sr^{2+} cations over the M1–M3 sites with temperature. Temperature dependencies of the monoclinic unit-cell parameters and the volume of $\text{Nd}(\text{Ca}_{1-x}\text{Sr}_x)_4\text{O}(\text{BO}_3)_3$, $x = 0.0, 0.2$ and 0.5 , were approximated independently using quadratic polynomials in the temperature range $25\text{--}800^\circ\text{C}$, in which no phase transformations occur (Table S10). Thermal expansion coefficients along principal axes of the tensor and its orientation in the monoclinic plane defined by μ_{1a} angle equal to the angle between α_{11} and a axis, as well as coefficients along crystallographic axes and volume for $\text{Nd}(\text{Ca}_{1-x}\text{Sr}_x)_4\text{O}(\text{BO}_3)_3$ ($x = 0, 0.2, 0.5$) solid solutions, are given in Table 3.

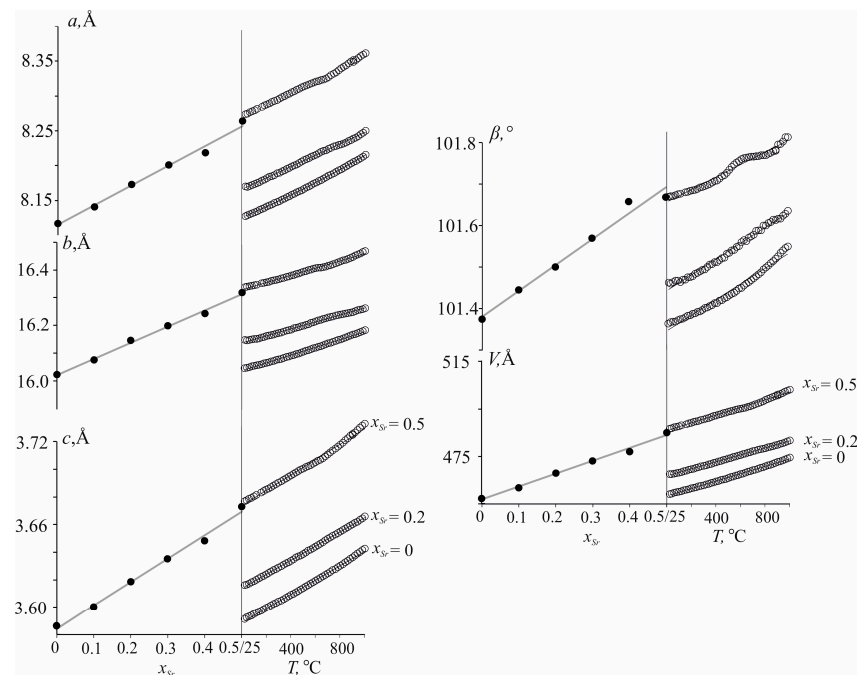


Figure 4. Dependencies of unit-cell parameters of the $\text{Nd}(\text{Ca}_{1-x}\text{Sr}_x)_4\text{O}(\text{BO}_3)_3$ versus chemical composition (left) and temperature (right). E.s.d. for the cell parameters is comparable with the size of the data points.

Table 3. Thermal expansion coefficients α ($\times 10^{-6} \text{ }^\circ\text{C}^{-1}$) along principal axes of tensor and along crystallographic axes for $\text{Nd}(\text{Ca}_{1-x}\text{Sr}_x)_4\text{O}(\text{BO}_3)_3$ ($x = 0, 0.2, 0.5$).

x	α_{11}	α_{22}	α_{33}	μ_{1a}	μ_{3c}	α_a	α_c	α_β	α_V
$T = 25 \text{ }^\circ\text{C}$									
0	9.02	6.94	11.38	21.1	9.7	9.33	11.31	0.668	27.35
0.2	10.22	7.46	13.17	26.09	15.5	10.83	12.96	1.10	30.85
0.5	8.41	6.59	11.51	31.1	19.5	9.24	11.17	1.32	26.52
$T = 400 \text{ }^\circ\text{C}$									
0	9.78	8.38	14.04	26.9	15.5	10.65	13.74	1.59	32.2
0.2	9.22	7.83	14.19	25.5	14.0	10.15	13.90	1.75	31.24
0.5	9.36	7.41	14.12	22.5	10.8	10.06	13.95	1.44	30.89
$T = 600 \text{ }^\circ\text{C}$									
0	10.14	9.10	15.38	28.2	16.8	11.30	14.94	2.05	34.61
0.2	8.69	8.02	14.73	25.2	13.6	9.77	14.40	2.09	31.45
0.5	9.82	7.84	15.54	20.1	8.4	10.49	15.41	1.51	33.19
$T = 800 \text{ }^\circ\text{C}$									
0	10.48	9.81	16.70	29.2	17.7	11.96	16.13	2.51	36.99
0.2	9.56	8.29	15.48	24.9	13.1	9.33	14.94	2.77	31.65
0.5	10.28	8.20	16.94	18.1	6.0	11.03	16.89	1.67	35.87

The structures expand to their maximum along the α_{33} axis of the thermal expansion tensor, which is close to the c axis, where edge-shared chains of $M1$ – $M3$ polyhedra extend in parallel in the cationic framework of the structure. Almost perpendicular to the c axis, the planes of the BO_3 triangles are also located, which may be the reason for the greater expansion of the structure perpendicular to the planes of the triangles in accordance with the principles of high-temperature crystallochemistry of borates [48].

3.3.2. Compositional Properties

In Figure 4, the compositional deformations of the $\text{Nd}(\text{Ca}_{1-x}\text{Sr}_x)_4\text{O}(\text{BO}_3)_3$ oxoborates are compared with the thermal expansion using the procedure developed by Filatov [46]. Compositional dependencies of the cell parameters for $\text{Nd}(\text{Ca}_{1-x}\text{Sr}_x)_4\text{O}(\text{BO}_3)_3$ were approximated linearly within 0–0.5: $a = 8.1133(44) + 0.0292(14)x$, $b = 16.0241(58) + 0.0586(16)x$, $c = 3.5844(22) + 0.01709(69)x$, $\beta = 101.391(11) + 0.0583(4)x$, $V = 456.7560 + 5.4970980x$. The linear equations for temperature dependence of the $\text{Nd}(\text{Ca}_{0.5}\text{Sr}_{0.5})_4\text{O}(\text{BO}_3)_3$ unit-cell parameters were: $a = 8.27172(31) + 0.00008213(65)t$, $b = 16.333360(45) + 0.00012072(96)t$, $c = 3.67479(19) + 0.00005123(39)t$, $\beta = 101.6544(23) + 0.1545(51)t$, $V = 486.2392 + 0.0150446t$ (Figure 4). The compositional and thermal expansions of $\text{Nd}(\text{Ca}_{0.5}\text{Sr}_{0.5})_4\text{O}(\text{BO}_3)_3$ lead to similar changes in the linear (a , b and c) and angular (β) parameters and the V volume, as well as in the principal axes of both tensors and their orientation. Thus, the structure of the $\text{Nd}(\text{Ca}_{0.5}\text{Sr}_{0.5})_4\text{O}(\text{BO}_3)_3$ solid solution of RCOB family type undergoes similar distortions upon heating (Figure 4, right side) and with increasing the Sr^{2+} ion content in $\text{Nd}(\text{Ca}_{1-x}\text{Sr}_x)_4\text{O}(\text{BO}_3)_3$ (Figure 4, left side). Eigenvalues (γ_{11} , γ_{22} , γ_{33}) of the tensor of the compositional deformation, γ_{aver} and γ_V are given in Table 4. For compositional deformations μ_{1a} , the angle between α_{11} and a axis equal to 27° is comparable with the same angle (23 – 27° of the thermal expansion tensor (Table 4).

Table 4. Thermal (α) and compositional (γ) deformation coefficients and their equivalents (α/γ) for $\text{NdCa}_4\text{O}(\text{BO}_3)_3$, $\text{Nd}(\text{Ca}_{0.8}\text{Sr}_{0.2})_4\text{O}(\text{BO}_3)_3$ and $\text{Nd}(\text{Ca}_{0.5}\text{Sr}_{0.5})_4\text{O}(\text{BO}_3)_3$.

Formula	Coefficient Tensor					Region				
	α_{11}	α_{22}	α_{33}	μ_{1a}	α_{aver}	α_V	T ($^\circ\text{C}$)			
Main parameters of the thermal expansion tensor α ($\times 10^6$ $^\circ\text{C}^{-1}$)										
$\text{NdCa}_4\text{O}(\text{BO}_3)_3$	9.78 (7)	9.2	8.45 (6)	14.06 (10)	27.2	25.9	10.38	32.3 (2)	31.4	20–800
$\text{Nd}(\text{Ca}_{0.8}\text{Sr}_{0.2})_4\text{O}(\text{BO}_3)_3$	(3)		7.97 (26)	14.20 (46)		23.1	10.32	(10)		20–800
$\text{Nd}(\text{Ca}_{0.5}\text{Sr}_{0.5})_4\text{O}(\text{BO}_3)_3$	9.10 (6)		7.35 (5)	13.98 (9)			10.14	30.4 (2)		20–800
Coefficient tensor								Region		
	γ_{11}	γ_{22}	γ_{33}	μ_{1a}	γ_{aver}	γ_V	x , at% Sr			
Main parameters of the compositional deformation tensor γ ($\times 0.01$ /at% Sr)										
$\text{Nd}(\text{Ca}_{0.5}\text{Sr}_{0.5})_4\text{O}(\text{BO}_3)_3$	32.01(1)	35.75(1)	47.44(2)	27.0	38.69	115.20(5)	0–0.5			
Coefficient tensor								Region		
	$(\alpha/\gamma)_{11}$	$(\alpha/\gamma)_{22}$	$(\alpha/\gamma)_{33}$		$(\alpha/\gamma)_{\text{aver}}$	$(\alpha/\gamma)_V$				
Compositional equivalents of the thermal expansion: α/γ ($\times 10^{-6}$ $^\circ\text{C}^{-1}$ /0.01 at% Sr)										
$\text{Nd}(\text{Ca}_{0.5}\text{Sr}_{0.5})_4\text{O}(\text{BO}_3)_3$	0.28	0.21	0.295		0.262	0.264	20–800			

For quantitative comparison, one can use the compositional equivalent of the thermal expansion, α/γ (0.01 at% Sr/ $^\circ\text{C}$) [46]. The average compositional equivalent of the thermal expansion of the $\text{Nd}(\text{Ca}_{0.5}\text{Sr}_{0.5})_4\text{O}(\text{BO}_3)_3$ structure is calculated to be 0.00026 at% Sr/ $^\circ\text{C}$ (Table 4, $(\alpha/\gamma)_{\text{aver}} = \alpha_V$). This means that heating $\text{Nd}(\text{Ca}_{0.5}\text{Sr}_{0.5})_4\text{O}(\text{BO}_3)_3$ by 1 $^\circ\text{C}$ leads to the same deformations as increasing the Sr^{2+} ion content in the compounds by 0.26 at%. The closeness of $(\alpha/\gamma)_{11}$, $(\alpha/\gamma)_{22}$ and $(\alpha/\gamma)_{33}$ (0.28, 0.21 and 0.29 at%/ $^\circ\text{C}$) to the average value (0.26 at%/ $^\circ\text{C}$) indicates a high degree of similarity of the deformations occurring with changes in temperature and chemical composition.

3.3.3. Temperature-Dependent Structural Evolution of $\text{Nd}(\text{Ca}_{0.8}\text{Sr}_{0.2})_4\text{O}(\text{BO}_3)_3$ Solid Solution from Single-Crystal XRD Data

To expand our knowledge of the structure response to increasing temperature, we investigated the temperature-dependent structural behavior of $\text{Nd}(\text{Ca}_{0.8}\text{Sr}_{0.2})_4\text{O}(\text{BO}_3)_3$ solid solution in the range of 300–1273 K. First, we examine the thermal redistribution of Nd, Ca and Sr cations over $M1$ – $M3$ positions. It turned out that the redistribution of cations does not exceed 5–10%.

The thermal expansion of unit-cell parameters of the solid solution is discussed in Section 3.3.2 and here we present data on the thermal expansion of bonds in the $\text{Nd}(\text{Ca}_{0.8}\text{Sr}_{0.2})_4\text{O}(\text{BO}_3)_3$ solid solution. Individual and average bond lengths increase with temperature (Figure S4, Table S9). Changes in individual bond lengths vary from 0.012 Å to 0.072 Å. As a rule, stronger increases offer enough long bond lengths; for example, in an M1O_6 octahedron (M1—O6) bond, the length equal to 2.515 Å at room temperature increases by 0.072 Å, for others see Table S9. In spite of the difference in oxygen atoms surrounding the M1—M3 positions (C.N. range from six to eight), the change in the average $\langle \text{M—O} \rangle$ distances with temperature is almost the same for all of the polyhedra (approximately 0.003 Å between 300 K and 1273 K) (Figure 3, right, Table S9). The coefficients of thermal expansion calculated for average distances of the M—O bond lengths are $\langle \alpha_{\text{M1—O}} \rangle = 13.2 \times 10^{-6} \text{ }^\circ\text{C}^{-1}$, $\langle \alpha_{\text{M2—O}} \rangle = 14.0 \times 10^{-6} \text{ }^\circ\text{C}^{-1}$, $\langle \alpha_{\text{M3—O}} \rangle = 13.0 \times 10^{-6} \text{ }^\circ\text{C}^{-1}$. These values are in good agreement to data for average distances of the M—O bonds equal to $\langle \alpha_{\text{Ca}[\text{CN } 6]\text{—O}} \rangle = 13.8 \times 10^{-6} \text{ }^\circ\text{C}^{-1}$ for Ca, $\langle \alpha_{\text{Sr}[\text{CN } 6]\text{—O}} \rangle = 13.8 \times 10^{-6} \text{ }^\circ\text{C}^{-1}$ and $\langle \alpha_{\text{Sr}[\text{CN } 8]\text{—O}} \rangle = 16.4 \times 10^{-6} \text{ }^\circ\text{C}^{-1}$ from [45,49].

In the oxy-centered tetrahedra, O1M_4 bond lengths weakly increase with temperature increasing (Figure 3, right, Table S9). Thermal expansion calculated for an average distance of the O1—M bond length is $\langle \alpha_{\text{M1—O}} \rangle = 9 \times 10^{-6} \text{ }^\circ\text{C}^{-1}$ that is one and a half times less than the $\langle \alpha_{\text{M—O}} \rangle$ in M1—M3 polyhedra. This indicates more significant rigidity in this group.

Individual B—O bond lengths within $[\text{BO}_3]$ triangular groups practically do not change with temperature, and even most of them decrease slightly (Table S9). The average B—O bond lengths are also almost constant with temperature: the changes in the $\langle \text{B—O} \rangle$ lengths are -0.002 and -0.007 Å (Figure 3, right, Table S9). This contraction of bond lengths seems to be an artifact of the X-ray diffraction method. The effect of thermal motion on the estimation of bond lengths from a diffraction experiment is well known and described in detail [47,48,50,51]. The B—O bonds seem to be a very rigid group, as the whole vibrates as a rigid body motion that leads to a slight decrease of the boron–oxygen distances with a temperature increase from XRD data. The refinement of the anisotropic parameters of thermal vibrations for the O atoms demonstrates that the vibration amplitudes increase approximately twice (1.9–2.5). Groups are located in a preferred orientation that dictates the anisotropy of thermal expansion in the direction perpendicular to plane triangles (Figure 3, right).

3.4. Melting Processes of $\text{Nd}(\text{Ca}_{1-x}\text{Sr}_x)_4\text{O}(\text{BO}_3)_3$ Solid Solutions from DCS Data

DSC curves on heating of $\text{Nd}(\text{Ca}_{1-x}\text{Sr}_x)_4\text{O}(\text{BO}_3)_3$ samples demonstrate strong thermal endothermic effects corresponding to melting processes (Figure 5): onset temperatures for homogeneous solid solutions melting ($x = 0\text{--}0.5$) decreased from 1389 °C to 1246 °C (1389, 1356, 1299, 1267, 1266, 1246 °C for $x = 0, 0.1, 0.2, 0.3, 0.4$ and 0.5 , respectively) as well as the temperature of maximum endothermic effects from 1455 °C to 1316 °C (1455, 1427, 1386, 1363, 1336 and 1316 °C) as Ca is replaced by Sr. This is due to the fact that the strength of the Ca—O bonds is shorter and therefore weaker than the Sr—O bond strength; therefore, with an increase in the content of Sr ions, a decrease in the temperature of solid solutions can be expected. The peaks corresponding to the melting of solid solutions are broadened, especially for $x = 0.2$ and 0.3 (Figure 5), due to melting processes occurring in a two-phase region—here recrystallization in the presence of a liquid phase takes place. Overlapping peaks can be split, as in samples with $x = 0.1$ and 0.2 , where the first weak peaks (1396 and 1344 °C for $x = 0.1$ and 0.2) might be attributed to solidus temperature while the strong peaks are to liquidus temperature. It is noteworthy that the difference in liquidus and solidus temperatures decreases to $x = 0.5$. Multiphase samples melt by eutectic reaction. In the case of insignificant second phase amounts, peaks appeared before strong peaks, such as in the sample with $x = 1$, where there are two peaks, a small one at 1209 °C according to the eutectic point and a strong one at 1291 °C—liquidus point—in the binary eutectic $\text{NdSr}_4\text{O}(\text{BO}_3)_3\text{—Sr}_3\text{B}_2\text{O}_6$ system. In the case of three phases existence,

first, apparently a small ternary eutectic mix melts at 1181 °C, then the endothermic effect at 1281 °C corresponds to liquidus temperature in the ternary system, and the endothermic effect at 1281 °C could be interpreted as liquidus temperature in the binary system (Figure 5).

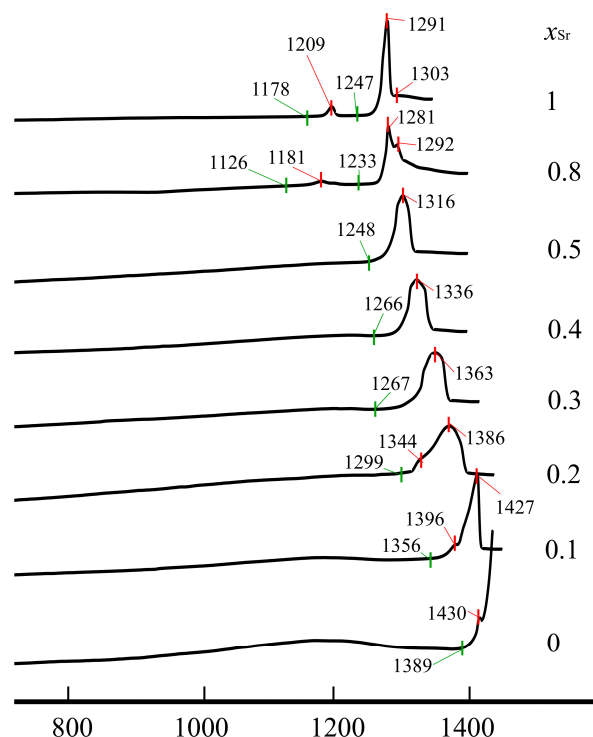


Figure 5. DCS heating curves of $\text{Nd}(\text{Ca}_{1-x}\text{Sr}_x)_4\text{O}(\text{BO}_3)_3$ samples after heat-treatment at 1300 °C.

On the cooling curves, crystallization occurs at a lower temperature due to hysteresis in the melting and crystallization temperatures. It is noteworthy that the hysteresis reaches a maximum in solid solutions up to 70–80 °C for $x = 0.2, 0.3$ and decreases in single chemical compounds and multiphase samples to 20–40 °C.

3.5. Raman Spectra

Raman spectra of the $\text{Nd}(\text{Ca}_{1-x}\text{Sr}_x)_4\text{O}(\text{BO}_3)_3$ samples are presented in Figure 6a. Peaks below 500 cm^{-1} associated with libration modes of the (BO_3) matrix units. The wide peak around 600 cm^{-1} corresponds to the bending vibrations of (BO_3) triangles. The most intensive peak in the region of 925 cm^{-1} is associated with symmetric stretching vibrations $\nu_s(\text{BO}_3)$ [52]. This peak consists of two bands, the position of the maxima of which shifts to the low-frequency region with an increase in the concentration of strontium in the samples (Figure 6b). The presence of two bands is probably due to two symmetrically independent boron atoms, as was shown in the structural part. In this case, with an increase in the Sr concentration, the position of both maxima shifts linearly towards low frequencies (Figure 6c). According to one of the theoretical models, the shift of the phonon band towards low frequencies can be associated with an increase in mass upon isovalent substitution in a solid solution [53]. For example, this shift is observed in $\text{Ca}_3(\text{BO}_3)_2$ and $\text{Sr}_3(\text{BO}_3)_2$ crystalline samples [54].

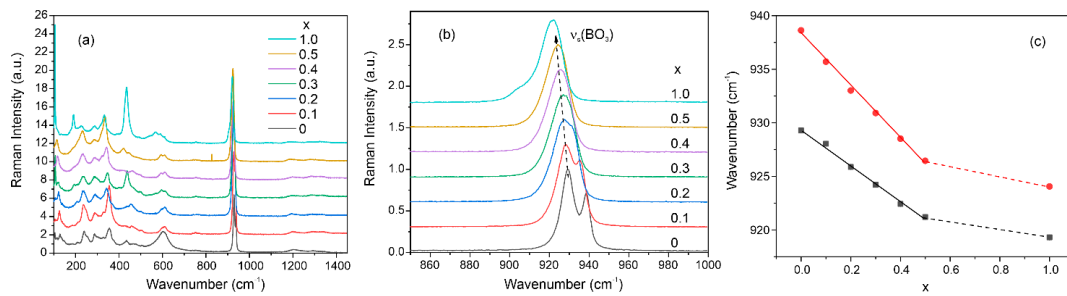


Figure 6. Raman spectra of $\text{Nd}(\text{Ca}_{1-x}\text{Sr}_x)_4\text{O}(\text{BO}_3)_3$ samples (a); $\nu_s(\text{BO}_3)$ peaks shift (b); dependencies of $\nu_s(\text{BO}_3)$ peaks maxima on the Sr concentration (c).

3.6. Optical Bandgap

The absorption spectra show a set of bands that all correspond to neodymium transitions (Figure 7a). It should be noted that the concentration of Nd^{3+} ions in the samples is so high that no luminescence is observed due to concentration quenching. In the spectral region below 250 nm, a blue edge of the transparency window is observed, which is associated with fundamental absorption. The position of the fundamental edge of optical absorption was used to determine the optical band gap using the Tauc plot graphics. It was found that there is a decrease in the optical band gap when calcium is substituted by strontium ions (Figure 7a). This is consistent with the theory of the influence of the mass of substituting ions on the band gap [53].

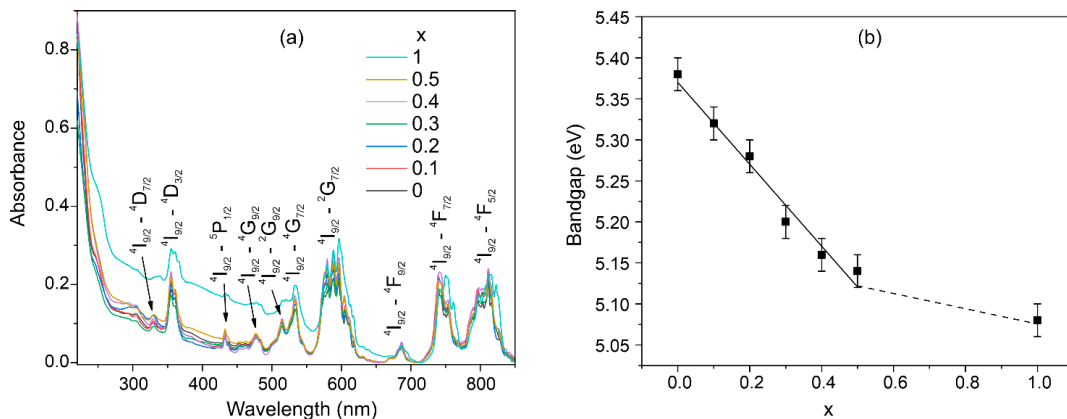


Figure 7. Absorption spectra of the $\text{Nd}(\text{Ca}_{1-x}\text{Sr}_x)_4\text{O}(\text{BO}_3)_3$ samples (a); dependence of optical bandgap on the Sr concentration (b).

3.7. Second Harmonic Generation

SHG signal was recorded for the $\text{Nd}(\text{Ca}_{1-x}\text{Sr}_x)_4\text{O}(\text{BO}_3)_3$ samples under otherwise equal conditions, which makes it possible to qualitatively estimate the efficiency of light conversion into the second harmonic of the investigated solid solutions (Figure 8a). The obtained experimental results show that the optical nonlinearity of the $\text{Nd}(\text{Ca}_{1-x}\text{Sr}_x)_4\text{O}(\text{BO}_3)_3$ crystals can be improved with partial substitution of Sr^{2+} ions for Ca^{2+} ions in the crystal up to $x = 0.2$. To determine the SHG efficiency, the obtained results were compared with the results of crystalline quartz with the same particle size distribution (Figure 8b). Obviously, the synthesized solid solutions demonstrate an order of magnitude better ability to generate the second harmonic compared to crystalline quartz, although the SHG response shown in Figure 8b is indeed not typical. This is most likely due to the peculiarities of the polycrystalline samples, where microparticles are agglomerates of smaller particles. Probably, in the samples with different sizes of granules, not all agglomerates were separated into individual particles, which led to the dependence of SHG response.

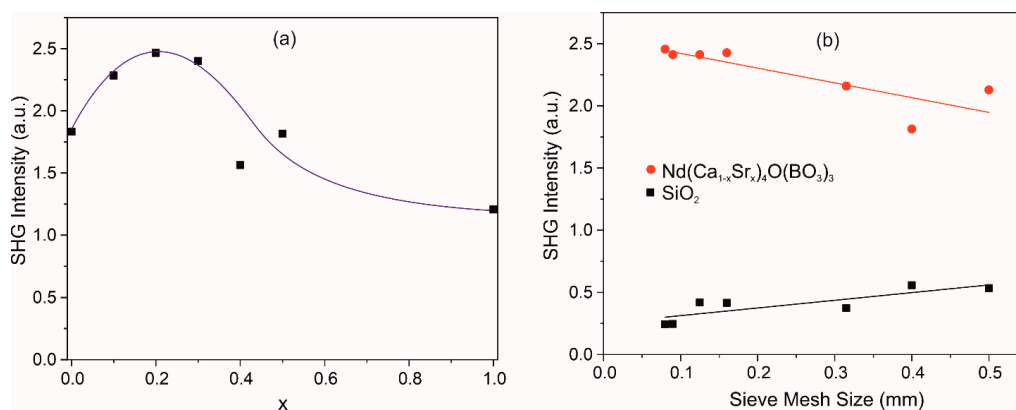


Figure 8. SHG signal dependence on Sr concentration for $\text{Nd}(\text{Ca}_{1-x}\text{Sr}_x)_4\text{O}(\text{BO}_3)_3$ samples (a); SHG signal dependencies as a function of particle size for $\text{Nd}(\text{Ca}_{0.8}\text{Sr}_{0.2})_4\text{O}(\text{BO}_3)_3$ and SiO_2 polycrystals as the reference (b).

Finally, consider the features of the structure that may affect the optical nonlinearity. In addition to the already reported factors improving the optical nonlinearity in this borate family, such as a partial substitution of Yb for Y in $\text{YCa}_4\text{O}(\text{BO}_3)_3$ [19] or doping of Sr for Ca in $\text{GdCa}_4\text{O}(\text{BO}_3)_3$ [22], we believe that, in accordance with the anion group theory [55–58], the significant contribution to the NLO properties originates also from the BO_3 groups that form delocalized π -type bonds perpendicular to the BO_3 plane. Accordingly, special attention is therefore paid in borates to the orientation of the triangular groups [48,58–60]. In this family $[\text{BO}_3]$, triangular groups are located at a small angle to each other (see Figure 3). Another relatively new crystal chemistry factor that can affect the optical nonlinearity is the additional oxygen atom, which is not bonded to the B atom. Its role in influencing the optical nonlinearity is not quite clear; however, its influence in [61] has already been noted, apparently for the first time. It is coordinated by metal atoms and forms a rigid $\text{O}1\text{M}_4$ tetrahedron, which leads to distortion of cationic M polyhedra. This situation is described in detail in the case of Ca–Sr substitution in GdCOB , similar to Ca–Sr substitution in NdCOB (see Section 3.2).

4. Conclusions

Novel non-centrosymmetric $\text{Nd}(\text{Ca}_{1-x}\text{Sr}_x)_4\text{O}(\text{BO}_3)_3$ solid solutions and a new $\text{NdSr}_4\text{O}(\text{BO}_3)_3$ compound with large second harmonic generation responses were synthesized by solid-state reactions and characterized by powder and single crystal X-ray diffraction in the wide range of temperatures. It turned out that Ca ions can be replaced by Sr ones up to approximately 70% which exceeds practically twice similar substitutions in the $\text{REE}(\text{Ca}_{1-x}\text{Sr}_x)_4\text{O}(\text{BO}_3)_3$ solid solution series ($x = 0.35$ for Gd and 0.4 for La). Moreover, a new non-centrosymmetric $\text{NdSr}_4\text{O}(\text{BO}_3)_3$ borate has been obtained and structurally characterized from single-crystal XRD data, which can be a prototype of a new $\text{LnSr}_4\text{O}(\text{BO}_3)_3$ series that may exhibit important properties for practical applications due to the features of the crystal structure.

The anisotropy of thermal expansion of $\text{Nd}(\text{Ca}_{1-x}\text{Sr}_x)_4\text{O}(\text{BO}_3)_3$ solid solutions with $x = 0, 0.2, 0.5$ is not very sharp ($\alpha_{\text{max}}/\alpha_{\text{min}} < 2$), it is apparently caused by thermal vibrations of rigid BO_3 groups perpendicular to the plane of groups in accordance with the principles of high-temperature crystal chemistry of borates. Anisotropy of thermal expansion of $\text{Nd}(\text{Ca}_{1-x}\text{Sr}_x)_4\text{O}(\text{BO}_3)_3$ solid solutions ($x = 0, 0.2, 0.5$) is similar to compositional deformations that occur during Ca–Sr substitutions, a compositional equivalent of the thermal expansion, α/γ (0.01 at% Sr/ $^\circ\text{C}$) was applied.

The experimental results showed that the optical nonlinearity of the $\text{Nd}(\text{Ca}_{1-x}\text{Sr}_x)_4\text{O}(\text{BO}_3)_3$ crystals can be improved by the partial substitution of Sr^{2+} ions for Ca^{2+} ions up to $x = 0.2$ in the structure. Crystal chemistry basis may contribute to this: location of plain BO_3

groups, distortions of M polyhedra as a result of Ca-Sr substitutions, existence of additional oxygen atoms tetrahedrally coordinated by M metal ions.

Supplementary Materials: The following supporting information can be downloaded at: <https://www.mdpi.com/article/10.3390/cryst13091395/s1>. Figure S1. XRD patterns of the Nd(Ca_{1-x}Sr_x)₄O(BO₃)₃ solid solutions synthesized at 1300 °C; Figure S2. 2D-top view of HTXRD pattern of the sample Nd(Ca_{0.5}Sr_{0.5})₄O(BO₃)₃. The dotted line indicates the beginning of the appearance of the impurity; Figure S3. Microstographs of the planchette in the form of NdCa₄O(BO₃)₃ before (left) and after (right) heating to 1445 °C; Figure S4. Changes of bond lengths in the cationic M1–M3 polyhedra and oxy-centered OM₄ tetrahedra (top left) with increasing temperature; Table S1. Atomic coordinates, isotropic or equivalent isotropic displacement parameters (Å²) in the structure of Nd(Ca_{0.8}Sr_{0.2})₄O(BO₃)₃; Table S2. Atomic coordinates, isotropic or equivalent isotropic displacement parameters (Å²) and in the structure of Nd(Ca_{0.5}Sr_{0.5})₄O(BO₃)₃; Table S3. Atomic coordinates, isotropic or equivalent isotropic displacement parameters (Å²) and in the structure of NdSr₄O(BO₃)₃; Table S4. Atomic displacement parameters (Å²) for Nd(Ca_{0.8}Sr_{0.2})₄O(BO₃)₃; Table S5. Atomic displacement parameters (Å²) for Nd(Ca_{0.5}Sr_{0.5})₄O(BO₃)₃; Table S6. Atomic displacement parameters (Å²) for NdSr₄O(BO₃)₃; Table S7. Bond lengths (Å) of Nd(Ca_{1-x}Sr_x)₄O(BO₃)₃ (x = 0.2, 0.5, 1); Table S8. Crystal data and experimental details for structures of Nd(Ca_{0.8}Sr_{0.2})₄O(BO₃)₃ in the temperature range 300–1273 K; Table S9. Change in bond lengths (Å) of Nd(Ca_{0.8}Sr_{0.2})₄O(BO₃)₃ in the temperature range 273–1273 K; Table S10. Coefficients of approximation of temperature dependencies by polynomial function ($p_T = p_0 + p_1T + p_2T^2$) of Nd(Ca_{1-x}Sr_x)₄O(BO₃)₃ (x = 0, 0.2, 0.5) solid solutions.

Author Contributions: Writing—original draft, R.B., V.Y. and A.P.; Writing—review and editing, M.K., S.F., R.B. and V.Y.; Investigation, A.Y., M.K., A.P., S.V. and V.U.; Project administration, R.B.; Data curation, V.Y., R.B. and S.F.; Visualization, A.Y., A.P., V.U. and V.Y.; Supervision, R.B. All authors have read and agreed to the published version of the manuscript.

Funding: This work was supported by the Russian Science Foundation [grant number 22-23-01133] (data evaluation and generalization, XRD and NLO-investigation, Raman and absorption spectroscopy) and the Ministry of Science and Higher Education of the Russian Federation within the scientific tasks of the Institute of Silicate Chemistry (Russian Academy of Sciences) [project number 0081-2022-0002] (synthesis).

Data Availability Statement: CCDC 2286252, 2286231 and 2286250 contain the crystallographic data for this paper. These data can be obtained free of charge via <https://www.ccdc.cam.ac.uk/Community/Depositastructure/CSDCommunications/> (accessed on 2 August 2023).

Acknowledgments: The X-ray diffraction experiments were performed at the Centre for X-ray Diffraction Studies (Saint Petersburg State University). The Raman spectra and NLO-measurements were collected at the Center for Optical and Laser Materials Research, Research Park of Saint-Petersburg State University.

Conflicts of Interest: The authors declare no conflict of interest.

References

1. Khamaganova, T.N.; Trunov, V.K.; Dzuhrinskii, B.F. The crystal structure of calcium samarium oxide borate Ca₈Sm₂O₂(BO₃)₆. *Russ. J. Inorg. Chem.* **1991**, *36*, 484–485.
2. Norrestam, R.; Nygren, M.; Bovin, J.-O. Structural investigations of new calcium-rare earth (R) oxyborates with the composition Ca₄RO(BO₃)₃. *Chem. Mater.* **1992**, *4*, 737–743. [\[CrossRef\]](#)
3. Ilyukhin, A.B.; Dzhurinskii, B.F. Crystal structures of binary oxoborates LnCa₄O(BO₃)₃ (Ln = Gd, Tb, and Lu) and Eu₂CaO(BO₃)₂. *Russ. J. Inorg. Chem.* **1993**, *38*, 847–850.
4. Sasaki, T.; Mori, Y.; Yoshimura, M.; Yap, Y.K.; Kamimura, T. Recent development of nonlinear optical borate crystals: Key materials for generation of visible and UV light. *Mater. Sci. Eng. R* **2000**, *30*, 1–54. [\[CrossRef\]](#)
5. Aka, G.; Kahn-Harari, A.; Vivien, D.; Benitez, J.M.; Salin, F.; Godard, J. A new non-linear and neodymium laser self-frequency doubling crystal with congruent melting: Ca₄GdO(BO₃)₃ (GdCOB). *Eur. J. Solid State Inorg. Chem.* **1996**, *33*, 727–736. [\[CrossRef\]](#)
6. Iwai, M.I.M.; Kobayashi, T.K.T.; Furuya, H.F.H.; Mori, Y.M.Y.; Sasaki, T.S.T. Crystal growth and optical characterization of rare-earth (Re) calcium oxyborate ReCa₄O(BO₃)₃ (Re = Y or Gd) as new nonlinear optical material. *Jpn. J. Appl. Phys.* **1997**, *36*, L276. [\[CrossRef\]](#)
7. Aka, G.; Kahn-Harari, A.; Mougél, F.; Vivien, D.; Salin, F.; Coquelin, P.; Damelet, J.P. Linear and nonlinear-optical properties of a new gadolinium calcium oxoborate crystal, Ca₄GdO(BO₃)₃. *J. Opt. Soc. Am. B* **1997**, *14*, 2238–2247. [\[CrossRef\]](#)

8. Adams, J.J.; Ebberts, C.A.; Schaffers, K.I.; Payne, S.A. Nonlinear optical properties of $\text{LaCa}_4\text{O}(\text{BO}_3)_3$. *Opt. Lett.* **2001**, *26*, 217–219. [[CrossRef](#)]
9. Druon, F.; Balembois, F.; Georges, P.; Brun, A.; Courjaud, A.; Hönninger, C.; Vivien, D. Generation of 90-fs pulses from a mode-locked diode-pumped Yb^{3+} : $\text{Ca}_4\text{GdO}(\text{BO}_3)_3$ laser. *Opt. Lett.* **2000**, *25*, 423–425. [[CrossRef](#)]
10. Vincent, B.; Boudrioua, A.; Loulergue, J.C.; Moretti, P.; Tascu, S.; Jacquier, B.; Vivien, D. Channel waveguides in $\text{Ca}_4\text{GdO}(\text{BO}_3)_3$ fabricated by He+ implantation for blue-light generation. *Opt. Lett.* **2003**, *28*, 1025–1027. [[CrossRef](#)]
11. Chai, B.H. Advances in bulk inorganic nonlinear optical materials. *Opt. Phot. News* **1999**, *10*, 31. [[CrossRef](#)]
12. Kuz'micheva, G.M.; Kaurouva, I.A.; Rybakov, V.B.; Podbel'skiy, V.V. Crystallochemical design of huntite-family compounds. *Crystals* **2019**, *9*, 100. [[CrossRef](#)]
13. Kuz'micheva, G.M.; Ageev, A.Y.; Rybakov, V.B.; Panyutin, V.L.; Yu, Y.M.; Chizhikov, V.I. Growth and X-ray diffraction study of $\text{YCa}_4\text{O}(\text{BO}_3)_3$: Ce, Er, Yb crystals. *Inorg. Mater.* **2001**, *37*, 1051–1060. [[CrossRef](#)]
14. Yang, H.C.; Li, C.Y.; He, H.; Tao, Y.; Xu, J.H.; Su, Q. VUV–UV excited luminescent properties of $\text{LnCa}_4\text{O}(\text{BO}_3)_3$: RE^{3+} ($\text{Ln} = \text{Y, La, Gd}$; $\text{Re} = \text{Eu, Tb, Dy, Ce}$). *J. Lumin.* **2006**, *118*, 61–69. [[CrossRef](#)]
15. Furuya, H.; Nakao, H.; Yamada, I.; Ruan, Y.F.; Yap, Y.K.; Yoshimura, M.; Mori, Y.; Sasaki, T. Alleviation of photoinduced damage in $\text{Gd}_x\text{Y}_{1-x}\text{Ca}_4\text{O}(\text{BO}_3)_3$ at elevated crystal temperature for noncritically phase-matched 355-nm generation. *Opt. Lett.* **2000**, *25*, 1588–1590. [[CrossRef](#)] [[PubMed](#)]
16. Umemura, N.; Nakao, H.; Furuya, H.; Yoshimura, M.; Mori, Y.; Sasaki, T.; Yoshida, K.; Kato, K. 90° phase-matching properties of $\text{YCa}_4\text{O}(\text{BO}_3)_3$ and $\text{Gd}_x\text{Y}_{1-x}\text{Ca}_4\text{O}(\text{BO}_3)_3$. *Jpn. J. Appl. Phys.* **2001**, *40*, 596. [[CrossRef](#)]
17. Wang, Z.; Xu, X.; Fu, K.; Song, R.; Wang, J.; Wei, J.; Liu, Y.; Shao, Z. Non-critical phase matching of $\text{Gd}_x\text{Y}_{1-x}\text{Ca}_4\text{O}(\text{BO}_3)_3$ ($\text{Gd}_x\text{Y}_{1-x}\text{COB}$) crystal. *Solid State Commun.* **2001**, *120*, 397–400. [[CrossRef](#)]
18. Nakao, H.; Kawamura, K.; Furuya, H.; Yamada, I.; Yoshimura, M.; Mori, Y.; Sasaki, T. Investigation of the Gd variation of $\text{Gd}_x\text{Y}_{1-x}\text{Ca}_4\text{O}(\text{BO}_3)_3$ crystal and its application. *Jpn. J. Appl. Phys.* **2002**, *41*, L723. [[CrossRef](#)]
19. Jang, W.; Ye, Q.; Hammons, D.; Eichenholz, J.; Lim, J.; Richardson, M.; Chai, B.H.T.; Van Stryland, E. Improved Second-Harmonic Generation by Selective Yb Ion Doping in a New Nonlinear Optical Crystal YCOB. *IEEE J. Quant. Electr.* **1999**, *35*, 1826–1833.
20. Kelly, N.D.; Savvin, S.; Dutton, S.E. Crystal structure and specific heat of calcium lanthanide oxyborates $\text{Ca}_4\text{LnO}(\text{BO}_3)_3$. *Z. Kristallogr.* **2022**, *237*, 317–327. [[CrossRef](#)]
21. Möckel, R.; Reuther, C.; Götze, J. REECOB: 20 years of rare earth element calcium oxoborates crystal growth research. *Cryst. Growth Des.* **2013**, *371*, 70–76. [[CrossRef](#)]
22. Liu, J.; Wang, Z.; Zhang, S.; Wang, J.; Chen, H.; Shao, Z.; Jiang, M. Second-harmonic generation of $1.06 \mu\text{m}$ in Sr doped $\text{GdCa}_4\text{O}(\text{BO}_3)_3$ crystal. *Opt. Commun.* **2001**, *195*, 267–271. [[CrossRef](#)]
23. Achim, A.; Gheorghe, L.; Voicu, F.; Stanciu, G. Blue light production by type-I non-critical phase matching second-harmonic generation in $\text{La}(\text{Ca}_{1-x}\text{Sr}_x)_4\text{O}(\text{BO}_3)_3$ single crystals. *Cryst. Eng. Comm.* **2015**, *17*, 4098–4101. [[CrossRef](#)]
24. Weigel, T.; Mehner, E.; Stöcker, H.; Meyer, D.C.; Götze, J.; Hanzig, J. Crystal Structure of $\text{Gd}(\text{Ca}_{3.319}\text{Sr}_{0.681})\text{O}[\text{BO}_3]_3$ and $\text{Gd}(\text{Ca}_{2.592}\text{Sr}_{1.408})\text{O}[\text{BO}_3]_3$. *Cryst. Res. Technol.* **2023**, *58*, 2200255. [[CrossRef](#)]
25. Shannon, R.D. Revised effective ionic radii and systematic studies of interatomic distances in halides and chalcogenides. *Acta Crystallogr. Sect. A Found. Crystallogr.* **1976**, *32*, 751–767. [[CrossRef](#)]
26. Münchhalfen, M.; Schreuer, J.; Reuther, C.; Mehner, E.; Stöcker, H. Elastic, piezoelectric, and dielectric properties of rare-earth calcium oxoborates $\text{RCa}_4\text{O}(\text{BO}_3)_3$ ($\text{R} = \text{Er, Y, Dy, Gd, Sm, Nd, La}$). *J. Appl. Phys.* **2021**, *130*, 095102. [[CrossRef](#)]
27. Mougel, F.; Kahn-Harari, A.; Aka, G.; Pelenc, D. Structural and thermal stability of Czochralski grown GdCOB oxoborate single crystals. *J. Mater. Chem.* **1998**, *8*, 1619–1623. [[CrossRef](#)]
28. Dirksen, G.E.; Blasse, G. Tetracalcium gadolinium oxoborate ($\text{Ca}_4\text{GdO}(\text{BO}_3)_3$) as a new host lattice for luminescent materials. *J. Alloys Compd.* **1993**, *191*, 121–126. [[CrossRef](#)]
29. Zhang, Y.; Li, Y. Photo-luminescent properties of Eu^{3+} ion-doped $\text{Ca}_4\text{REO}(\text{BO}_3)_3$ ($\text{RE} = \text{La, Y, Gd}$). *J. Lumin.* **2005**, *113*, 45–49. [[CrossRef](#)]
30. Kuo, T.W.; Chen, T.M. Synthesis and luminescence of $\text{Ca}_4\text{YO}(\text{BO}_3)_3$: Eu^{3+} for fluorescent lamp application. *Opt. Mater.* **2010**, *32*, 882–885. [[CrossRef](#)]
31. Ju, G.; Hu, Y.; Chen, L.; Wang, X.; Mu, Z.; Wu, H.; Kang, F. The luminescence of bismuth and europium in $\text{Ca}_4\text{YO}(\text{BO}_3)_3$. *J. Lumin.* **2012**, *132*, 717–721. [[CrossRef](#)]
32. Yu, F.; Zhang, S.; Zhao, X.; Guo, S.; Duan, X.; Yuan, D.; Shrout, T.R. Investigation of the dielectric and piezoelectric properties of $\text{ReCa}_4\text{O}(\text{BO}_3)_3$ crystals. *J. Phys. D Appl. Phys.* **2011**, *44*, 135405. [[CrossRef](#)]
33. Münchhalfen, M.; Schreuer, J.; Reuther, C.; Möckel, R.; Götze, J.; Mehner, E.; Stöcker, H.; Meyer, D. Order/disorder processes and electromechanical properties of monoclinic $\text{GdCa}_4\text{O}(\text{BO}_3)_3$. *Z. Kristallogr.* **2019**, *234*, 707–723. [[CrossRef](#)]
34. Kelly, N.D.; Dutton, S.E. Magnetic properties of quasi-one-dimensional lanthanide calcium oxyborates $\text{Ca}_4\text{LnO}(\text{BO}_3)_3$. *Inorg. Chem.* **2020**, *59*, 9188–9195. [[CrossRef](#)] [[PubMed](#)]
35. Kalakkodu, S. *ICDD, PDF-2 2011, Database*; ICDD: Newtown Square, PA, USA, 2011.
36. Bubnova, R.S.; Firsova, V.A.; Volkov, S.N.; Filatov, S.K. RietveldToTensor: Program for processing powder X-ray diffraction data under variable conditions. *Glass Phys. Chem.* **2018**, *44*, 33–40. [[CrossRef](#)]
37. Palatinus, L.; Chapuis, G. SUPERFLIP—A computer program for the solution of crystal structures by charge flipping in arbitrary dimensions. *J. Appl. Crystallogr.* **2007**, *40*, 786–790. [[CrossRef](#)]

38. Petříček, V.; Dušek, M.; Palatinus, L. Crystallographic Computing System JANA2006: General features. *Z. Kristallogr. Cryst. Mater.* **2014**, *229*, 345–352. [[CrossRef](#)]
39. VESTA: Visualization for Electronic and Structural Analysis. Available online: <https://jp-minerals.org/vesta/en/> (accessed on 17 November 2021).
40. Zhang, Y.; Chen, X.L.; Liang, J.K.; Cao, Y.G.; Xu, T. Phase relations in the system $\text{La}_2\text{O}_3\text{--CaO--B}_2\text{O}_3$. *J. Alloys Compd.* **2001**, *315*, 198–202. [[CrossRef](#)]
41. Reuther, C.; Moeckel, R.; Hengst, M.; Goetze, J.; Schwarzer, A.; Schmidt, H. Growth and structure of $\text{Ca}_4\text{La}[\text{O}(\text{BO})_3]_3$. *J. Cryst. Growth* **2011**, *320*, 90–94. [[CrossRef](#)]
42. Crossno, S.K. Tetracalcium Lanthanide Borate Oxide: Structures and Optical Properties. Master's Thesis, Oregon State University, Corvallis, ON, USA, 1997.
43. Filatov, S.K. Nekotoryye strukturno-geometricheskiye izmereniya deformatsiy kristallov pri ispol'zovanii temperatury, davleniya i khimizm. *Kristallogr. Kristallokh.* **1973**, *2*, 5.
44. Hazen, R.M. Temperature, pressure, and composition: Structurally analogous variables. *Phys. Chem. Miner.* **1977**, *1*, 83–94. [[CrossRef](#)]
45. Hazen, R.M.; Finger, L.W. *Comparative Crystal Chemistry*; John Wiley & Sons: New York, NY, USA, 1982; Volume 231.
46. Filatov, S.K. *Vysokotemperaturnaya kristalloghimiya*; Nedra: Leningrad, Russia, 1990; Volume 288.
47. Hazen, R.M.; Downs, R.T.; Prewitt, C.T. Principles of comparative crystal chemistry. *Rev. Mineral. Geochem.* **2000**, *41*, 1–33. [[CrossRef](#)]
48. Bubnova, R.S.; Filatov, S.K. High-temperature borate crystal chemistry. *Z. Kristallogr.* **2013**, *228*, 395–428. [[CrossRef](#)]
49. Hazen, R.M.; Prewitt, C.T. Effects of temperature and pressure on interatomic distances in oxygen-based mineral. *Amer. Miner.* **1977**, *62*, 309–315.
50. Cruickshank, D.W.J. Errors in bond lengths due to rotational oscillations of molecules. *Acta Cryst.* **1956**, *9*, 757–758. [[CrossRef](#)]
51. Busing, W.R.; Levy, H.A. The effect of thermal motion on the estimation of bond lengths from diffraction measurements. *Acta Cryst.* **1964**, *17*, 142–146. [[CrossRef](#)]
52. Biryukov, Y.P.; Bubnova, R.S.; Krzhizhanovskaya, M.G.; Filatov, S.K.; Povolotskiy, A.V.; Ugolkov, V.L. Thermal behavior of polymorphic modifications of LuBO_3 . *Solid State Sci.* **2020**, *99*, 106061. [[CrossRef](#)]
53. Yasseri, M.; Schüpfer, D.; Chen, L.; Kamila, H.; Müller, E.; de Boor, J.; Klar, P.J. Raman Spectroscopic Study of the Optical Phonons of $\text{Mg}_2\text{Si}_{1-x}\text{Sn}_x$ Solid Solutions. *Phys. Status Solidi.* **2020**, *14*, 1900574. [[CrossRef](#)]
54. Wang, X.; Qi, H.; Li, Y.; Yu, F.; Wang, H.; Chen, F.; Zhao, X. Synthesis and characterization of new $\text{Sr}_3(\text{BO}_3)_2$ crystal for stimulated Raman scattering applications. *Crystals* **2017**, *7*, 125. [[CrossRef](#)]
55. Chen, C.; Sasaki, T.; Li, R.; Wu, Y.; Lin, Z.; Mori, Y.; Hu, Z.; Wang, J.; Uda, S.; Yoshimura, M.; et al. *Nonlinear Optical Borate Crystals: Principals and Applications*; John Wiley & Sons: New York, NY, USA, 2012; Volume 406.
56. Becker, P. Borate materials in nonlinear optics. *Adv. Mater.* **1998**, *10*, 979–992. [[CrossRef](#)]
57. Shen, Y.; Zhao, S.; Luo, J. The role of cations in second-order nonlinear optical materials based on π -conjugated $[\text{BO}_3]^{3-}$ groups. *Coord. Chem. Rev.* **2018**, *366*, 1–28. [[CrossRef](#)]
58. Gong, P.F.; Liu, X.M.; Kang, L.; Lin, Z.S. Inorganic planar π -conjugated groups in nonlinear optical crystals: Review and outlook. *Inorg. Chem. Front.* **2020**, *7*, 839–852. [[CrossRef](#)]
59. Mutailipu, M.; Poepplmeier, K.R.; Pan, S. Borates: A Rich Source for Optical Materials. *Chem. Rev.* **2021**, *121*, 1130–1202. [[CrossRef](#)]
60. Bubnova, R.; Volkov, S.; Albert, B.; Filatov, S.K. Borates—Crystal Structures of Prospective Nonlinear Optical Materials: High Anisotropy of the Thermal Expansion Caused by Anharmonic Atomic Vibrations. *Crystals* **2017**, *7*, 93. [[CrossRef](#)]
61. Bubnova, R.S.; Shablinskii, A.P.; Stefanovich, S.Y.; Arsent'ev, M.Y.; Krzhizhanovskaya, M.G.; Lazoryak, B.I.; Ugolkov, V.L.; Filatov, S.K. Expanding gaudefroyite family to $\text{Sr}_2\text{MBi}(\text{REEO})_3(\text{BO}_3)_4$ ($M = \text{Ca, Sr, Ba}$; $\text{REE} = \text{Y, Eu}$) borates with large second harmonic generation responses. *Ceram. Intern.* **2023**, *49*, 15082–15090. [[CrossRef](#)]

Disclaimer/Publisher's Note: The statements, opinions and data contained in all publications are solely those of the individual author(s) and contributor(s) and not of MDPI and/or the editor(s). MDPI and/or the editor(s) disclaim responsibility for any injury to people or property resulting from any ideas, methods, instructions or products referred to in the content.